Molecular Crystals and Liquid Crystals Science and Technology. Section A. Molecular Crystals and Liquid Crystals

Publication details, including instructions for authors and subscription information:
http://www.tandfonline.com/loi/gmcl19

Using X-ray Absorption Spectroscopy to Probe Structural Change in the Chemical Solid-State

Kevin J Roberts [a b]

[a] Department of Pure and Applied Chemistry, University of Strathclyde, 295 Cathedral Street, Glasgow, G1 1XL, UK

[b] SERC Daresbury Laboratory, Warrington, WA4 4AD, UK.

Version of record first published: 24 Sep 2006.

To cite this article: Kevin J Roberts (1994): Using X-ray Absorption Spectroscopy to Probe Structural Change in the Chemical Solid-State, Molecular Crystals and Liquid Crystals Science and Technology. Section A. Molecular Crystals and Liquid Crystals, 248:1, 207-242

To link to this article: http://dx.doi.org/10.1080/10587259408027181

Mol. Cryst. Liq. Cryst. 1994, Vol. 248, pp. 207–242
Reprints available directly from the publisher
Photocopying permitted by license only

Printed in the United States of America

USING X-RAY ABSORPTION SPECTROSCOPY TO PROBE STRUCTURAL CHANGE IN THE CHEMICAL SOLID-STATE

KEVIN J ROBERTS
Department of Pure and Applied Chemistry, University of Strathclyde, 295 Cathedral Street, Glasgow G1 1XL, UK and SERC Daresbury Laboratory, Warrington WA4 4AD, UK.

Abstract X-ray absorption spectroscopy (EXAFS and XANES) using synchrotron radiation offers a non-destructive technique capable of probing the local structural order around selected atomic species in materials. In addition, the intensity and penetrability afforded by the use of synchrotron sources means that real chemical systems can be examined *in-situ* without their removal from operating conditions as well as obviating the need for UHV environments. The basic principles associated with the generation of synchrotron radiation and of the technique of X-ray absorption spectroscopy are overviewed and illustrated through a number of examples. Future trends are also outlined.

INTRODUCTION

Recent years have seen a growing awareness of the importance and utility of advanced structural characterisation techniques in aiding our understanding, definition and optimisation of advanced material systems and processes. In this, X-ray based techniques are most useful in that they are non-destructive and can provide essential information concerning bulk and surface micro-structure over a wide range of atomic correlation length scales. Within this perspective X-ray absorption spectroscopy (EXAFS and XANES) using synchrotron radiation is finding increasing utility as it offers a technique capable of probing the local structural order around selected atomic species in materials. In addition, the intensity and penetrability afforded by the use of such sources means that real chemical systems can be examined *in-situ* without their removal from operating conditions as well as obviating the need for UHV environments.

In this paper, the basic principles associated with the generation of synchrotron radiation and of the technique of X-ray absorption spectroscopy are overviewed and illustrated through a number of case examples taken from studies [see also 1-4] carried out by the Strathclyde group over the past 5 years. No attempt has been made by the author, due to space limitations, to review work beyond this perspective. This work is

part of the general and wide ranging aim of the Strathclyde and Daresbury groups which focuses on a desire to be able to understand, predict, control and optimise the structural nature of chemical interfaces operating under realistic conditions. In this schematic synchrotron radiation has, in our view, made a number of novel and unique contributions to the field.

SYNCHROTRON RADIATION

Synchrotron radiation is produced when charged particles are accelerated to relativistic (ca. GeV) energies [5] in an electron storage ring. The electromagnetic radiation produced by this process, as shown in figure 1, spans the spectral range from hard X-rays through to infra-red radiation. Synchrotron radiation beams provide:

(a) a high intensity (ie some 10^2 - 10^4 times higher [6] than conventional sources) which allows for fast data collection thus enabling dynamic studies to be made;

(b) a high photon energy (as high as 50-100 keV) which allow for the penetration of interfacial structures thus enabling *in-situ* studies to be carried out.

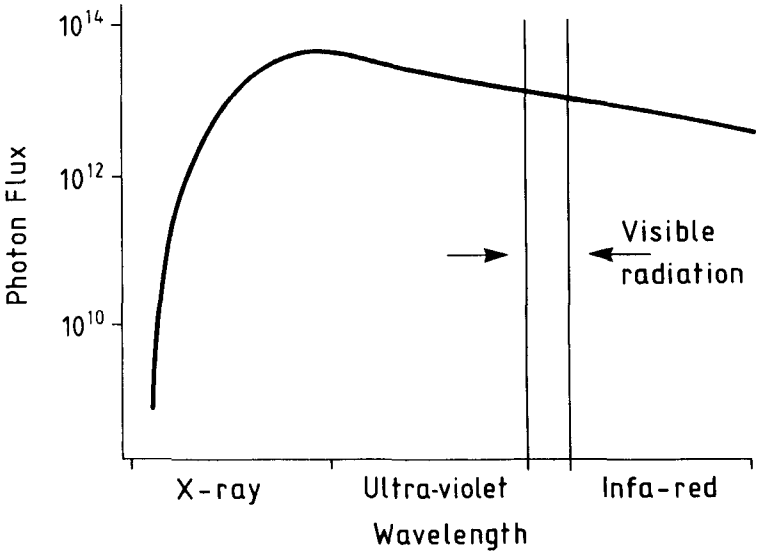

FIGURE 1. Synchrotron Radiation: the wavelength versus intensity profile of emitted synchrotron radiation as given from Wiggler beamline 9 at the Science and Engineering Research Council's synchrotron radiation source (SRS) at SERC Daresbury Laboratory in the UK.

X-RAY ABSORPTION SPECTROSCOPY

For spectroscopic studies the wide photon energy range of uniform intensity provided by synchrotron radiation enables the experimentalist to tune the photon energy of the synchrotron radiation beam to be close to the absorption edge of a given atomic species which can be utilised to probe the local atomic structural environment of the absorbing atom through X-ray absorption spectroscopy (XAS). As the absorption edges of elements in the periodic table ranging from P (ca. 2 keV) to Te (ca. 32 keV) are readily amenable to examination using synchrotron radiation spectrometers, XAS is a particularly effective tool for probing changes in the chemical state of mixed atom systems.

Basic Physical Principles

A schematic view of the basic physical principles underlying XAS [7-11] is summarised in figure 2. The X-ray absorption spectra taken of a condensed material exhibits an oscillatory structure which results from interference (a) between photoelectron waves generated by the absorption process which can extend up to 1000 eV or more (b) beyond the absorption threshold.

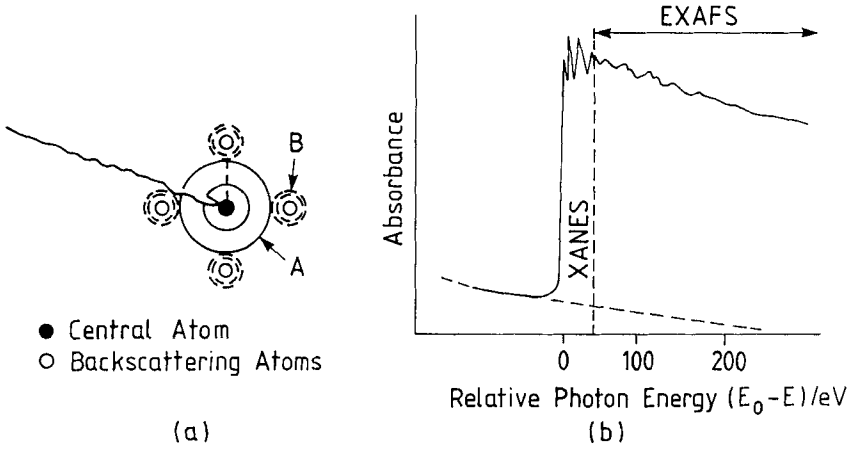

FIGURE 2. Schematic view of the basic physical principles underlying the technique of X-ray absorption spectrocopy: (a) the absorption process generates a photoelectron wave which propagates (A) in the material away from the absorbing atom and is partially backscattered (B) by the atomic near neighbours, resulting in interference between the outgoing and incoming waves; (b) this interference is observed as a periodic modulation on the high-energy side of the absorption threshold.

The features appearing close to the absorption edge can be attributed to transitions to localised electronic states and the edge position itself can be related to the oxidation state of the absorbing atom. These features together with the strong oscillations, the XANES (X-ray Absorption Near Edge Structure), which are observed just beyond the absorption

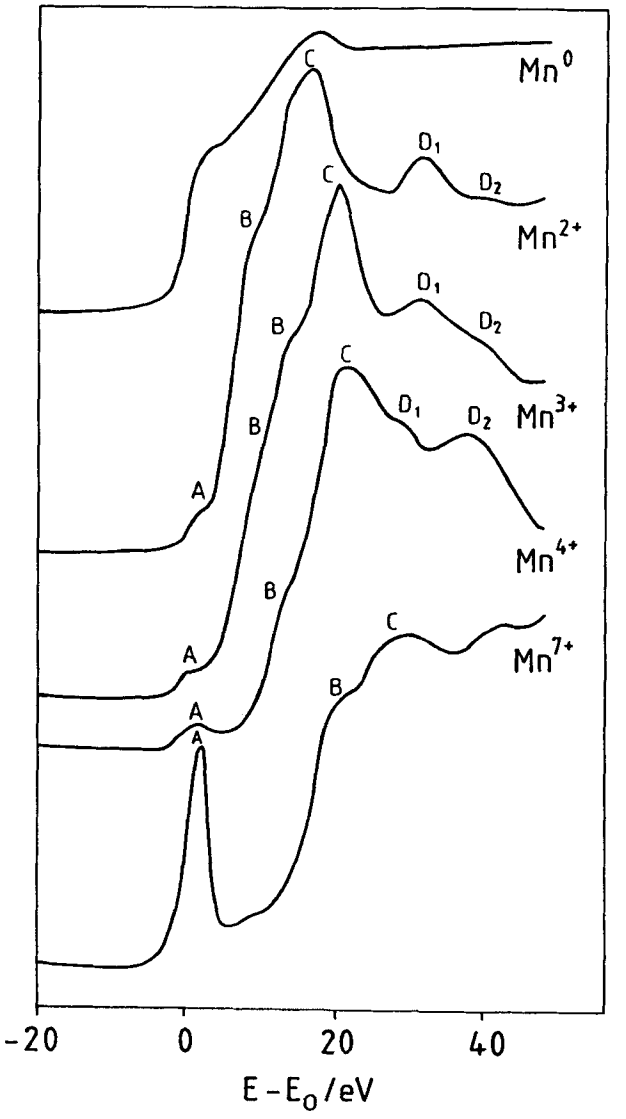

FIGURE 2(c). Mn K edge XANES (after [14], the absorption edge structure can give information on the geometrical arrangement of the near neighbouring atoms around the absorbing atom.

threshold provide a distinctive spectral "fingerprint" which enable different chemical states to be distinguished with confidence (c).

The structure observed from 30-40 eV beyond the edge, the EXAFS (Extended X-ray Absorption Fine Structure), is due to interference between the outgoing photoelectron wave and the wave as backscattered from the neighbouring atoms. These interference effects are determined by the distance, the chemical type and the number of atoms around the absorbing atom and since only elastically scattered electrons can interfere, and the elastic mean free path of electrons is short, the analysis of EXAFS structure provides information on the local atomic structure around the absorbing atom. As the EXAFS oscillations in the absorption cross-section can be decomposed (d) into a Fourier series of sinusoidal functions, one for each neighbour shell of neighbour atoms, a Fourier transform (e) of the spectra reveals the radial distribution function (RDF) of atomic sites with respect to the absorbing atom. Although single scattering is often sufficient to describe the EXAFS oscillations, there are specific cases where some multiple scattering (f) events need to be included in the interpretation of the experimental spectra.

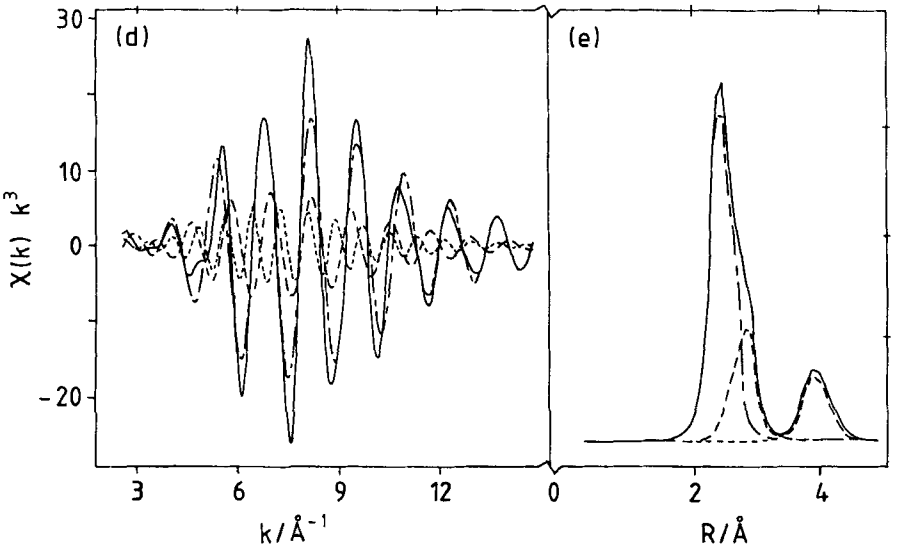

FIGURE 2. (d) EXAFS oscillations (———) in the absorption cross-section can be decomposed in a series of sinusoidal functions, one for each neighbour shell of neighbour atoms (1st shell (-- -- -- --), 2nd shell (-- - -- - --), 3rd shell (- - - - -)); (e) a Fourier transform of (d) reveals a RDF of atomic sites with respect to the absorbing atom, after [17].

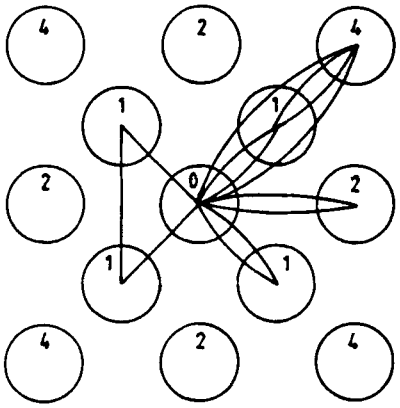

FIGURE 2(f). Schematic showing that in certain circumstances, single-scattering is not sufficient to fully describe the EXAFS and multiple-scattering paths have to be included, for example for a simple FCC structure the path 0 « 1 « 4 « 1 « 0 gives a strong contribution to the EXAFS because of the two forward scattering paths due to the first shell.

Analysis of EXAFS spectra can be carried out using standard procedures [7-11] which involve extraction of the EXAFS oscillations from the experimental XAS data using a cubic spline function to fit the atom-like background above the absorption edge. The background subtracted spectra is normalised to the absorption step height which is obtained by extrapolating the background absorption before and after the edge. In the so-called "plane wave approximation" the EXAFS function ($\chi(k)$) can be expressed by:

$$\chi(k) = \Sigma^i N_i k R_i^{-2} F_i(k) \exp(-2R_i/\lambda) \exp(-2k^2\sigma^2)\sin(2kR_i + \Phi_i) \quad (1)$$

where the summation is made over i coordination shells at an average distance R_i from the absorbing (central) atom and the coordination number N_i is the number of atoms at distance R_i. $F_i(k)$, the backscattering amplitude, strongly depends (g) on the type of scattering atom thus enabling the chemical nature of the backscatterer to be identified.

In general, atoms differing in atomic number by 2-3 can be discriminated with confidence using EXAFS. λ is the electron mean free path, σ_i is the root mean square deviation around the average distance R_i which appears as a Debye-Waller like factor, describing structural and thermal disorder. Φ_i is a phase shift term introduced by the fact that the wave function of the ejected photoelectron is modified by the potentials of the absorbing and backscattering atoms. These parameters can be fitted using curved wave theory (eg. using the computer program EXCURVE90 [13]) with the central atom

and backscattering phaseshifts being calculated *ab initio* and then checked for accuracy against the fits of the spectra of model compounds whose crystallographic structures are well known. Bond lengths (R) and coordination numbers (N) can typically be determined to a precision of about 10% and 0.01Å respectively.

Care must be exercised in understanding the numerical values of N where the number of surface atoms becomes significant with respect to the number of bulk atoms. In such cases (h) the coordination numbers are reduced with respect to those expected for a bulk system. Conversely, determination of N for well defined crystal phases can be used to estimate particle size.

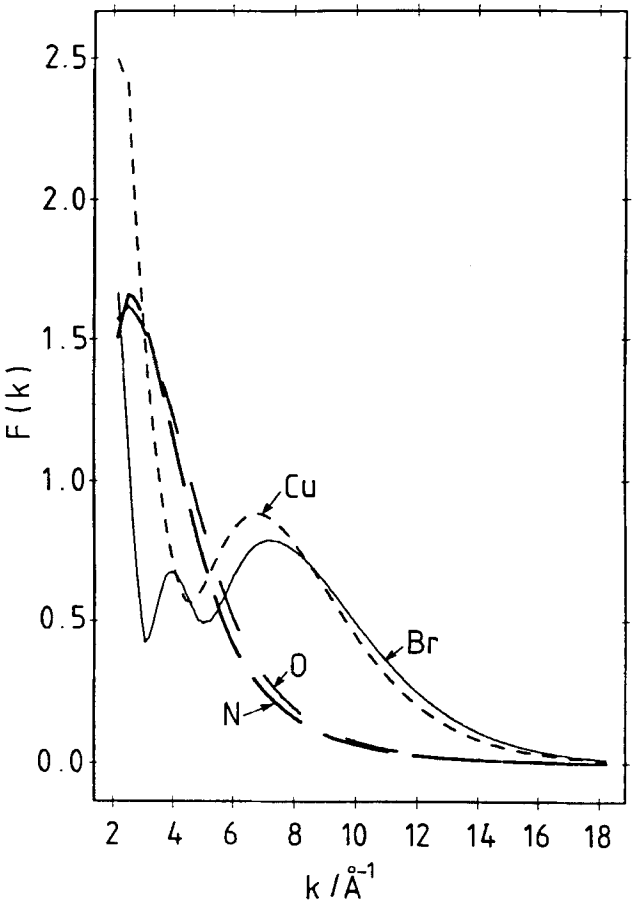

FIGURE 2(g) Calculated back-scattering amplitudes F(k) for Br, Cu, O and N atoms illustrating when atomic species can/cannot be discriminated using EXAFS.

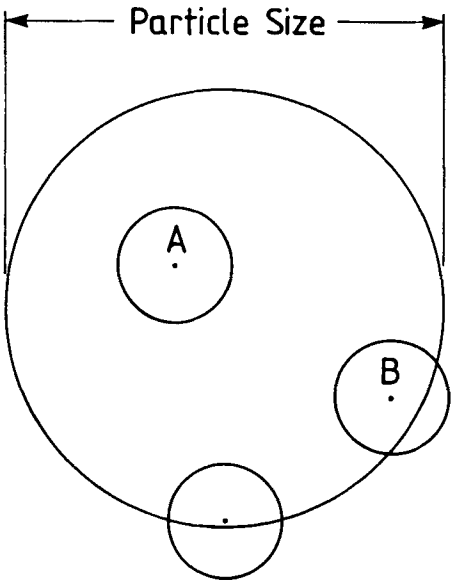

FIGURE 2(h) Schematic showing how a reduction in particle size can reduce the average measured coordination number.

Experimental Techniques

The experimental realisation of XAS spectra using synchrotron radiation, summarised in figure 3, requires the use of a monochromating crystal or grating to select the portion of the synchrotron radiation wavelength required to cover that spanning a range from ca. 50eV before the edge threshold to ca. 1000eV after the edge threshold. In order to provide a non-deviating monochromatic beam, a double crystal monochromator is typically used with the two crystals maintained slightly de-tuned [12] in order to reject contributions from higher harmonics. For studies of concentrated analytes, measurements can be carried out using transmission (using ion chambers for detection) or electron yield modes (a) with the samples in powdered form; typical data collection times are ca. 40 minutes. In the latter case, the measurements are made by recording the drain current from samples prepared by mixing the powdered material with a small amount of graphite and solvent and dispersing the mixture onto high purity copper substrates. For dilute analytes XAS spectra are typically recorded in fluorescence mode with the samples aligned at an angle of + 45° to the incident beam (b) and the data recorded using either a NaI(Th) scintillation counter or a liquid nitrogen cooled multi-

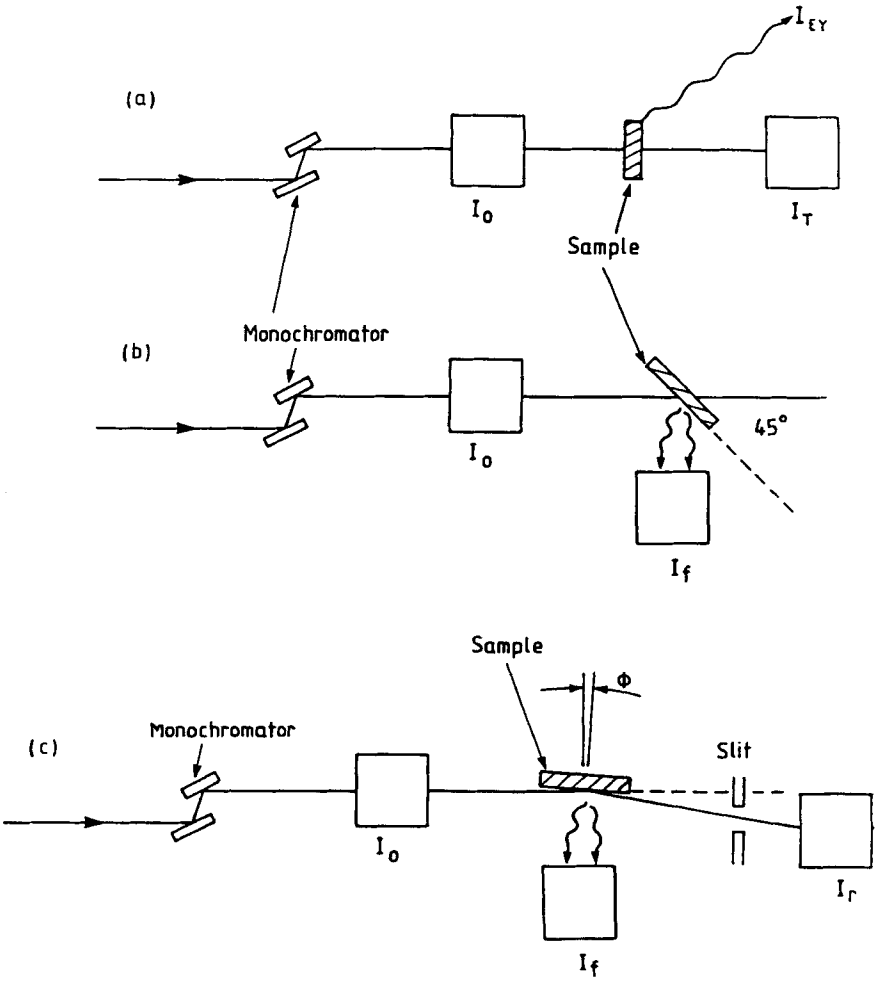

FIGURE 3. Sketch of the experimental set-up for X-ray absorption spectroscopy measurements: (a) experimental set-up for the collection of XAS spectra of bulk model compounds in which either the X-ray intensity transmitted through the sample (I_T) or the total electron yield measured by monitoring the sample drain current (I_{EY}) is measured as a function of photon energy with respect to the incident beam intensity (I_0); (b) experimental set-up for the collection of spectra from dilute analytes in which the fluorescence yield (I_f) is measured with respect to I_0 with the sample aligned at an angle of ca. 45° with respect to the incident beam; (c) surface sensitive glancing angle geometry in which spectra are measured with respect to I_0 either by monitoring the energy dependence of the reflected intensity (I_R) or the fluorescence intensity (I_F) as a function of glancing angle (f_c).

element Ge solid-state detector; data collection times in the range 1-10 hrs, depending on analyte concentration are typical. For studying the structural properties of surfaces and thin films, surface sensitivity can be achieved by working in glancing angle geometry using angles of incidence (ca. 0.2°) which are smaller than the critical angle for total external reflection. If the thickness of the surface complex is smaller than the minimum X-ray penetration depth (ca. 25Å) achievable in total reflection geometry, XAS spectra will no longer reflect only the surface complex, but will contain contributions from both the substrate and the surface layer. Data can be obtained by monitoring either the reflected intensity or the fluorescence signals.

SOME RECENT CASE STUDIES

In order to demonstrate the strength of XAS as a structural tool, the use of the various parameters important in data analysis and the range of chemical systems that can be examined with the technique, a number of case examples taken from recent work is presented. Full information on each system examined is given in the original cited papers.

The Surface Oxidation of a Polished GaAs (100) Wafer [15-17]

One of the problems in device preparation using compound semiconductors is that the surface oxides of group III-V materials have poorly understood and defined atomic structures when compared to group IV materials such as Si. As part of a study to examine the role of wafer polishing on subsequent material depositions, EXAFS in glancing mode was used to examine the structure of the "natural" surface oxide on a polished (100) GaAs wafer [15-17]. EXAFS spectra were recorded at glancing angles of incidence such that the penetration depth was about 30Å. Data was taken at the As K and Ga K absorption edges, so that the local structure around both atomic sites could be obtained separately. The results summarised in Table 1 and figure 4 show that the surface of the GaAs (100) wafer is partially oxidised which, from the ratio of the coordination numbers of bulk-like structures in the surface layer to those typical of GaAs, is indicative of an oxide thickness of ca. 8Å. The data also reveals that Ga and As atoms have different oxygen environments in the surface oxide. For both Ga and As atoms there is an oxygen neighbour shell at ca. 1.7Å, close to that found for the tetrahedral coordination in $GaAsO_4$. However, Ga atoms have an additional oxygen neighbour shell at ca. 1.95Å, which is typical of the octahedral coordination of Ga_2O_3. Thus, while As

atoms seem to be exclusively in a tetrahedral environment at the surface, Ga seems to be present in both tetrahedral and octahedral coordinations.

Material (edge)	R/Å (N)	R/Å (N)	R/Å (N)	R/Å (N)
Powdered GaAs (As)			As-Ga 2.45 (4.0)	As-As 3.99 (12.0)
Surface GaAs (Ga)	Ga-O 1.72 (0.6) 1.95 (2.2)	Ga-O-M 2.88 (3.1) 3.15 (3.4)	Ga-As 2.46 (3.0)	
Surface GaAs (As)	As-O 1.68 (0.9)	As-O-M 2.84 (1.1) 3.09 (1.0)	As-Ga 2.43 (3.1)	

TABLE 1. Coordination numbers (N) and coordination shell distances (R) extracted from the least-squares fits to As K edge data taken from powdered GaAs and from the surface of a (100) GaAs wafer; Ga K edge data taken from the surface of a (100) GaAs wafer, after [15-17].

The two complimentary cation shells (Ga or As) at the same distances (ca. 2.8Å and ca. 3.1Å for both Ga and As central atoms) are associated with the two different oxygen coordinations for Ga. The shells at ca. 2.8Å and at ca. 3.1Å are consistent with coordinations between cations both in a tetrahedral environment and octahedral Ga and a tetrahedral cation (As or Ga). The matching of these second shell distances for both Ga and As central atoms show the oxide to be a single component which can thus be modelled as a microscopically random mixture of tetrahedral and octahedral sites linked via oxygen bridges, with Ga occupying both and As only the former 4-fold site. A sketch of the structural model based on these results is shown in figure 5(a).

Comparison of the Ga and As environments as a function of incident angle (ie of depth) shows no significant variation for As concentration, whilst it indicates a distinct increase in Ga coordination at the surface. this trend indicatesa grwater association of Ga atoms to O in the outermost oxide layer and a corresponding As depletion. As structural model [16,17] of this oxide reveals an open structure with an atomic density much smaller than that of any of the crystalline oxides of Ga and/or As. The presence of 2-fold coordinated oxygens and the variable cation coordination combine to encourage the formation of micro-voids (typical size ca. 5Å) whose internal surfaces are oxygen rich

(figure 5(b)). Such a surface exhibits highly catalytic properties and has been found to actively promote the oxidation of any overlayers deposited on this surface [16,17].

This example has demonstrated the use of grazing incidence XAS which together with an analysis of EXAFS data at the Ga (10.37 keV) and As (11.87 keV) edges has been used to resolve the surface structure of monolayer quantities of oxide on GaAs.

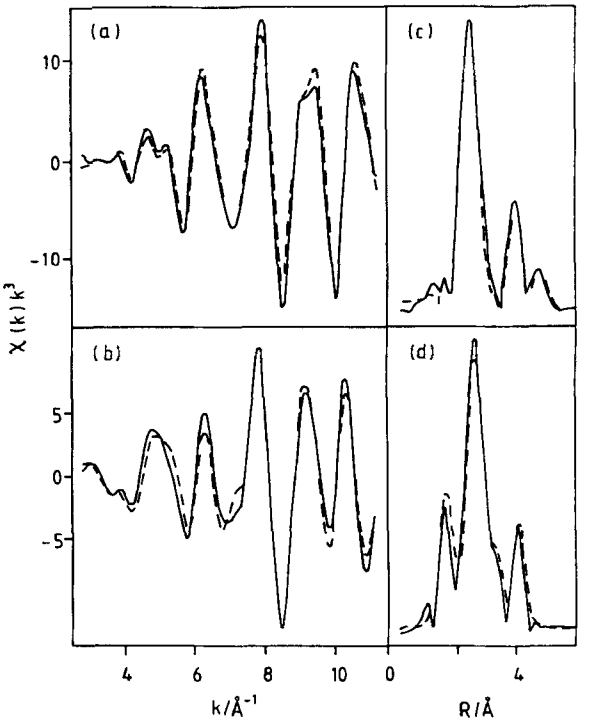

FIGURE 4. Experimental EXAFS data (——) together with corresponding least-squares fits (- - -) after [15-17], taken from: (a) GaAs powder (As K edge); (b) the (100) surface of a polished GaAs wafer (As K edge); (c) and (d) are the corresponding Fourier transforms.

The Structural Environment Around Cu^{2+} Habit Modifying Ions in Ammonium Sulphate [18-20]

The control of crystal shape is important in the chemical processing of solid crystalline particulates, as incorrectly defined and optimised crystal morphology can have a detrimental effect on crystal purity, filtration, storage, bioavailability etc. When crystallisation results in an undesirable crystal morphology, habit modifying additives can be used to control the relative growth rates of the crystal surfaces in order to optimise the desired particle shape. Such heterogeneous additives are presumed [21] to

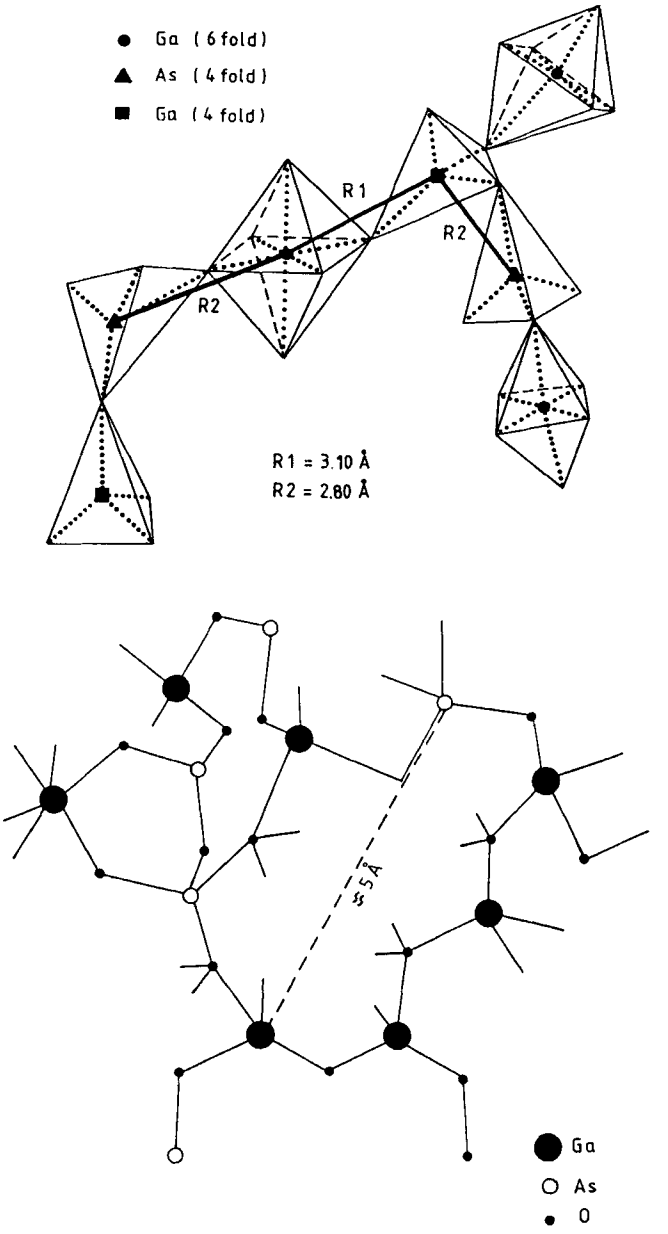

FIGURE 5. (a) Sketch of the local coordination of Ga and As atoms in the oxide coating on GaAs(100): 6-fold and 4-fold coordinated Ga atoms are linked to 4-fold coordinated As atoms *via* oxygen bridges, after [15]; (b) sketch of the section of a typical fissure in the oxide on GaAs(100), obtained from a three-dimensional molecular model of the oxide, after [17].

affect the growth rate of individual crystal faces by affecting the structure of the crystallised material by either blocking the movement of surface step/kink terraces or by incorporating in the solid-state and disrupting the intermolecular bonding networks. For ionic crystals, habit modifying additives often take the form of trace metal ions [22] for which XAS can be used to characterise the additive binding site geometry. This approach provides a powerful structural tool for the selection and definition of additive molecules, which is illustrated here in a recent study of the habit modification by Cu^{2+} ions of ammonium sulphate ($(NH_4)_2SO_4$).

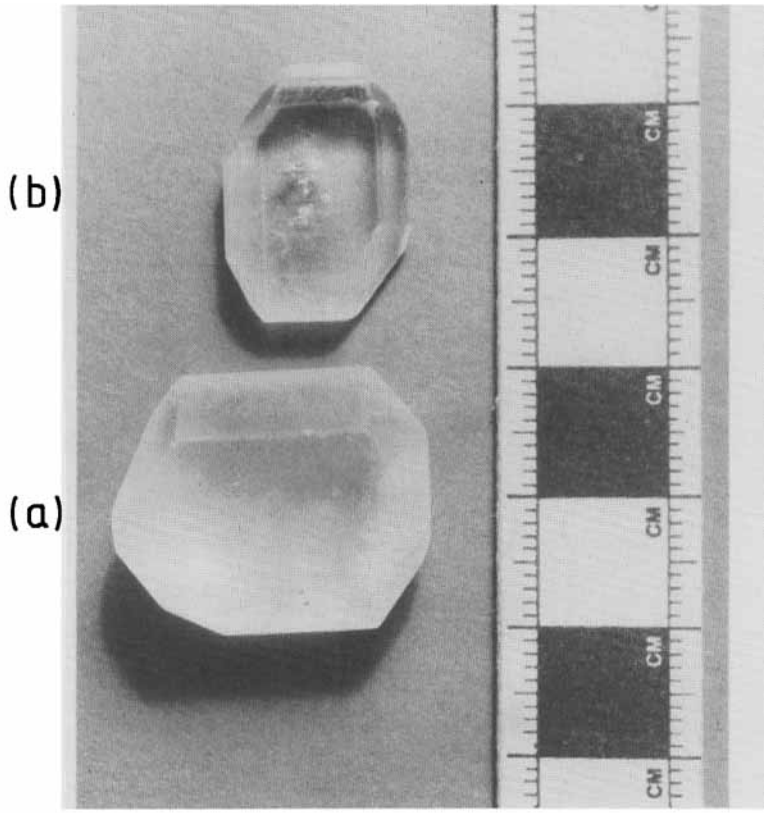

FIGURE 6. Photographs of typical "as-grown" crystals grown at a constant pH of 4, after [19,20]; (a) un-doped crystal; (b) crystal doped with ca. 5000 $\mu g.g^{-1}$ Cu^{2+} in the form of $CuSO_4.5H_2O$. The horizontal view is ca. 10cm.

Nearly perfect single crystals of ammonium sulphate were grown by solvent evaporation at 313 K from seeded saturated aqueous solutions (pH = 4) with and without the presence of ca. 5000 $\mu g.g^{-1}$ Cu^{2+} ions in the form of $CuSO_4.5H_2O$. The as-grown crystals exhibited a well-defined prismatic morphology, slightly elongated along the c-

axis (figure 6(a)) for the un-doped crystals and slightly elongated along the pseudo-hexagonal a-axis (figure 6(b)) for the doped crystals. Trace element analysis revealed the impurity to be uniformly incorporated within the crystal matrix. UV_{vis} spectroscopy, the light blue colouration of the doped crystals and the fact that the doping tended to remove solvent inclusions provided strong evidence for hydrated additive ions.

In the Cu K near-edge XAS spectra, shown in figure 7, it can be seen that the features in the Cu dopant ions in the crystal lattice are divalent, whilst analysis of the EXAFS spectra (Table 2) show that Cu^{2+} in the doped crystal is closely correlated to six

Sample	Atom	N	R/Å	σ^2/Å^2	Origin
Data from fits to the EXAFS spectra					
$CuSO_4.5H_2O$	O	2.2	1.18	0.003	H_2O
	O	3.3	2.07	0.006	H_2O
	O	1.2	2.34	0.031	SO_4
	O	0.6	2.45	0.031	SO_4
Cu^{2+} doped	O	2.3	1.86	0.008	H_2O
$(NH_4)_2SO_4$	O	2.5	1.95	0.008	H_2O
	O	2.1	2.57	0.031	SO_4
Crystallographic values					
$CuSO_4.5H_2O$	O	1.0	1.93		H_2O
	O	2.0	1.96		H_2O
	O	1.0	1.97		H_2O
	O	1.0	2.38		SO_4
	O	1.0	2.43		SO_4
$Cu(NH_4)_2$	O	2.0	1.94		H_2O
$(SO_4)_2.6H_2O$	O	2.0	2.07		H_2O
	O	2.0	2.23		H_2O

TABLE 2. Structural fits to the EXAFS data taken at the Cu K absorption edge, after [18-20], for $CuSO_4.5H_2O$ and $Cu^{2+}/(NH_4)_2SO_4$ together with the radial distribution functions derived from the crystal structures of ammonium copper pentahydrate ($CuSO_4.5H_2O$) [23] and Tutton's salt ($Cu(NH_4)_2(SO_4)_2.6H_2O$) [24].

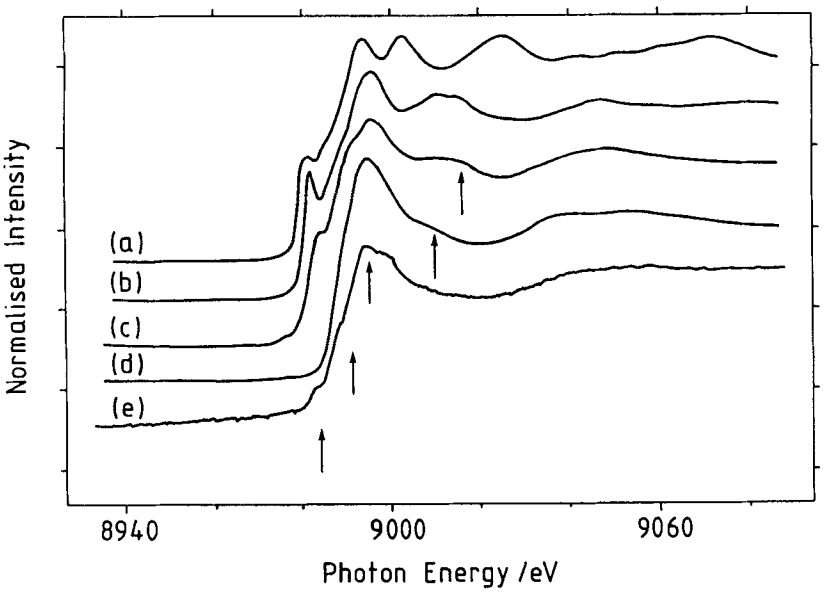

FIGURE 7. XANES spectra at the Cu K edge for the Cu^{2+} doped crystal and related model compounds, after [19]: (a) Cu metal; (b) Cu_2O; (c) CuO; (d) $CuSO_4.5H_2O$; (e) Cu^{2+} doped $(NH_4)_2SO_4$. The distinctive spectral features are arrowed.

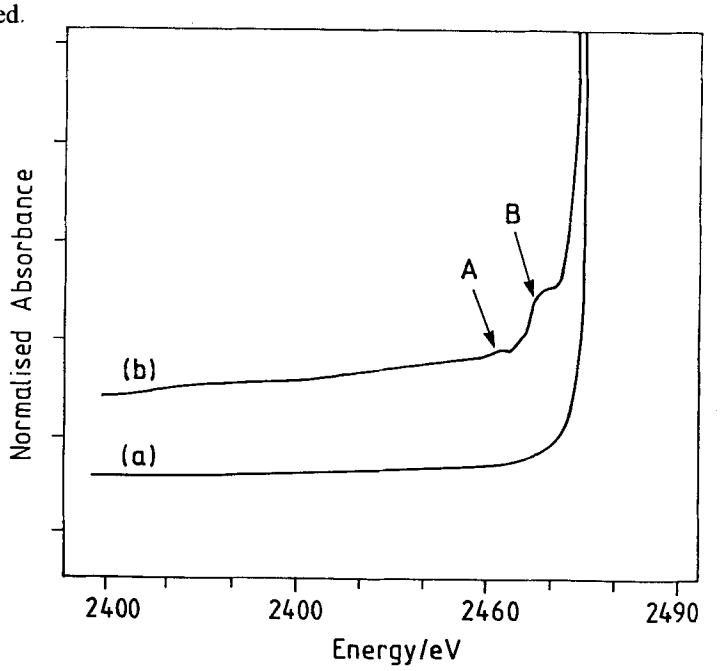

FIGURE 8. X-ray absorption near-edge spectra taken at the S K edge; (a) ammonium sulphate; (b) Cu^{2+} doped ammonium sulphate, after [19].

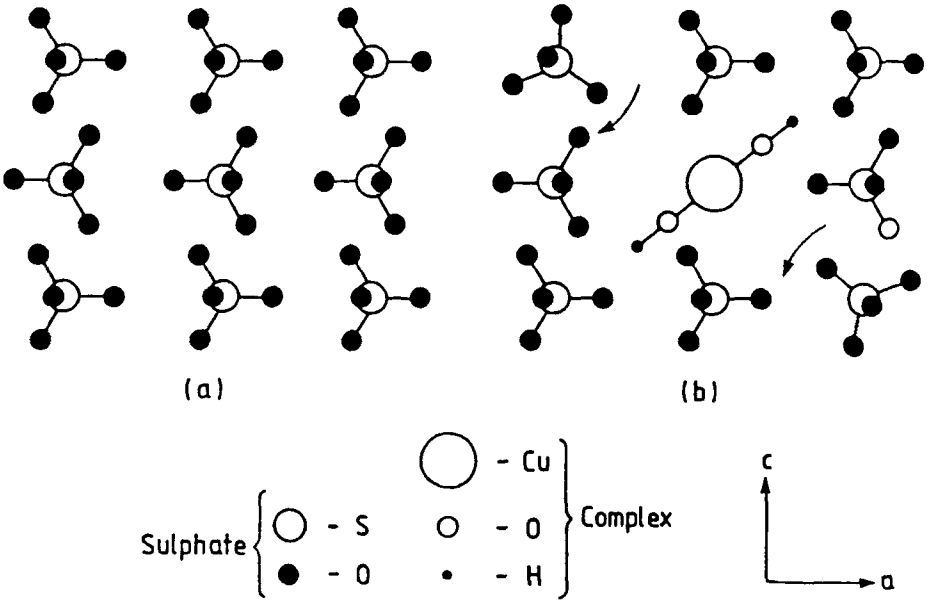

FIGURE 9. Projection of the crystal structure onto the (010) crystal plane showing the nature of the incorporation site, after [19]; (a) without Cu complex; (b) schematic showing the possible incorporation site and associated rotation of the sulphate anions. Note the ammonium ions have been removed for clarity.

SO_4^{2-}		NH_4^+		H_2O		$Cu(H_2O)_4^{2+}$		$Cu(H_2O)_6^{2+}$	
S	+1.60	N	-0.88			Cu	+1.35	Cu	+1.23
O	-0.90			O	-0.73	O	-0.81	O	-0.77
		H	+0.47	H	+0.37	H	+0.48	H	+0.45

TABLE 3. Results of the *ab initio* calculations, after [18-20] showing the predicted electronic charges on the SO_4^{2-} and NH_4^+ ions, H_2O and the $Cu(H_2O)_4^{2+}$ and $Cu(H_2O)_6^{2+}$ hydrated complexes.

oxygen atoms in a distorted octahedral configuration. The resulting radial distribution function is similar to that around Cu^{2+} in $CuSO_4.5H_2O$ [23] rather than that in Tutton's salt ($Cu(NH_4)_2(SO_4)_2.6H_2O$) [24] in that it appears strongly coordinated (ie. shorter bond lengths and small Debye-Waller factors) to four of the oxygen atomic sites in a

square planar arrangement, with weaker (ie. longer bond lengths and larger Debye-Waller factors) interactions with the two equatorial oxygen sites. If we take $CuSO_4.5H_2O$ as a model, then the former relate to coordinations with water molecules and the latter are coordinations to sulphate ions. Within the doped ammonium sulphate crystal the radial distribution of the axial atoms surrounding the Cu atom site differs from $CuSO_4.5H_2O$, in that there is a distortion of the square planar arrangement of ca. 0.1Å. The XAS spectra taken at the S K edge (figure 8) reveal weak pre-edge features 2464.7 eV (A) and 2470 eV (B). The transitions associated with such features are spectroscopically "pseudo-forbidden" being related to excitations from the 1s to 3d energy levels resulting, in this case, from a mixing between the 2p band of the host ammonium sulphate with vacant 3d states of the Cu complex. This shows that the dopant ions distort the tetrahedral site geometry of the sulphate group [25,26]. Therefore this result strongly supports the incorporation of the Cu dopant environment within the bulk solid-state structure, probably associated with disruption of the hydrogen-bonding network in the ammonium sulphate structure, resulting in a distortion of the tetrahedral symmetry.

In order to rationalise the experimental data, in particular how hydrated Cu^{2+} dopant cations can adsorb at or close to the anionic SO_4^{2-} sites in anhydrous ammonium sulphate, we used *ab initio* calculations to model Cu^{2+}/water interactions. The results, summarised in Table 5, show that the highly polarised nature of the Cu complexes allows the complexed water to mimic the electron distribution of the ammonium ions thus fulfilling the requirement for the molecular recognition of the dopant at the crystal growth interface. The overall structural model of the adsorption, shown in figure 9, is consistent with the hydrated Cu^{2+} complex occupying a lattice site centred on a SO_4^{2-} anion associated with the displacement of four additional NH_4^+ cations to maintain charge neutrality.

The loss of four strong inter-ion bonds associated with the complex incorporation into the crystal lattice does not, in itself, seem to affect the calculated surface attachment energies and hence explain the observed habit modification which appears to be due to the easier surface binding of the complex to the anion-rich pseudo-hexagonal{020} and {011} faces in the affected [100] crystal zone.

This example has demonstrated the use of fluorescence XAS (EXAFS and XANES) at the S (2.47 keV) and Cu (8.98 keV) K edges; this together with *ab initio* quantum chemistry calculations has been used to examine and quantify the local atomic environment around habit modifying Cu^{2+} ions in ammonium sulphate.

The Structure of Cu-Benzotriazole Complexes in Relation to their role in Corrosion Inhibition [17,27,28]

Whilst benzotriazole ($C_6N_3H_5$, BTA) is an efficient corrosion inhibitor for copper and its alloys [29], its mechanism of action is still unclear. It has been proposed [30] that the anti-corrosion mechanism is associated with the formation of an insoluble polymeric film consisting [31] of Cu(I)-BTA chains, in which Cu(I) would bind to one BTA unit by substitution of the N-H group hydrogen to another unit by the formation of a coordinate link to thelone pair of electrons of one of the nitrogens.

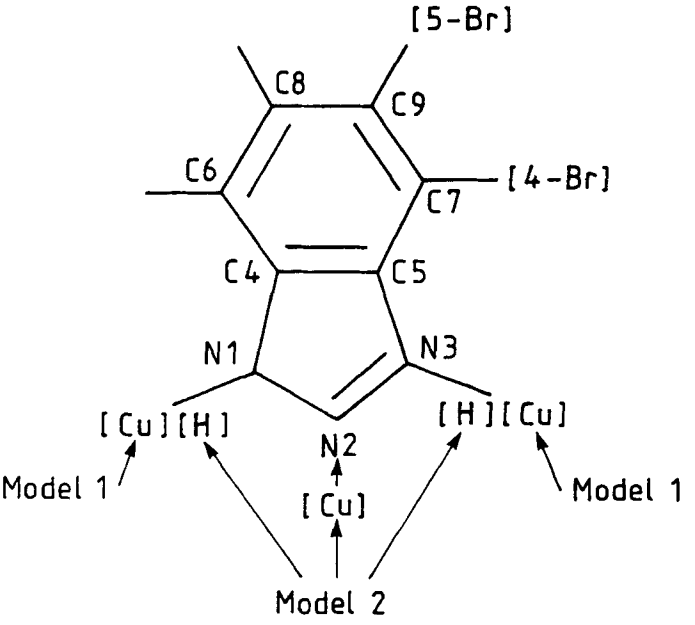

Figure 10. Schematic structural formula for benzotriazole and Cu-Br-BTA compounds. Bromine is in site [4-Br] in 4-Br-BTA and in site [5-Br] in 5-Br-BTA, after [28]. Copper can coordinate to N1 or N3 (model 1) or N2 (model 2).

The amorphous nature of these surface species make XAS an ideal structural tool for their characterisation. In this example, multiple scattering calculations together with bromo-substitution of hydrogen atom sites have been used to resolve the local atomic structure of this weakly backscattering surface complex. The schematic for this is shown in figure 10 from which we can postulate two hypothetical RDFs (Table 4) for the Cu-BTA binding ie. binding to sites N1/N3 (model 1) as in [31] or to N2 (model 2).

The Cu K edge experimental and fitted spectra for Cu(I)-BTA and Cu(I)-4-Br-BTA complexes are shown in figure 11. Both spectra are very similar thus demonstrating the

validity of using Br- substitution in this case. The EXAFS spectrum of Cu(I)-BTA, fitted using the RDFs derived from the two models as initial structures, revealed a best fit to model 2 (Table 4). Five atoms were included in the calculation, the nitrogen atom N2 at 2.00Å, and atoms N1, N3, C4 and C5, which contribute with single and multiple scattering to the spectra. In the analysis the carbon atom C6, essential in model 1, was not found to be statistically significant [32]. This analysis is supported by the analysis of the Cu(I)-4-Br-BTA data taken at both Cu and Br K edges [17,28] in which no evidence was found for the close Cu-Br or Br-Cu correlations expected for model 1.

The structural model based on this analysis, shown in figure 12(c), reveals the likely coordination geometry of the BTA molecules to a Cu surface. In this, the distance between adjacent Cu atoms would be ca. 4 Å which closely matches the second nearest neighbour Cu-Cu distance in Cu_2O at 4.25 Å. Such a model differs from that proposed by Cotton [31] (figure 12(a)) being more similar to that proposed by Fang et al. [33] (figure 12(b)) in that the structure involves the coordination of adjacent BTA molecules via hydrogen-bonds. However, the work of Fang et al suggested a Cu-BTA complex

Model 1			Model 2			Cu(I)-BTA				
Atom	r	α	Atom	r	α	Atom	r	α	$2\sigma^2$	N
N1	2.00		N2	2.00		N2	2.00		0.015	3.7
C4	2.98	-124	N1	2.98	-124	N1	2.87	-120	0.018	3.7
N2	2.97	+124	N3	3.04	+128	N3	3.02	+126	0.017	3.7
C6	3.51	-101								
N3	4.08	+160	C5	4.26	+163	C5	4.25	+162	0.015	3.7
C5	4.12	-163	C4	4.25	-161	C4	4.11	-155	0.017	3.7
C8	4.87	-115	C7	5.59	+159					
C7	5.39	-155	C6	5.54	-155					
C9	5.64	-135	C9	6.60	+173					
C8	6.59	-169								

TABLE 4. The calculated partial radial distribution functions around Cu for the two structural models for Cu(I)-BTA shown in figure 9 (model 1 and model 2), after [17,27,28] are compared with the structural parameters N, r (Å), α (°) and 2 σ^2 ($Å^2$) obtained from the best least-squares fits of the Cu K edge spectra of Cu(I)-BTA. In this α is the angle between the Cu-N bonding vector and the atom in question.

BTA complex binding to clean Cu surfaces involving two nitrogen atom (either N1/N2 or N2/N3) binding sites, justifying this through the close correlation of their models' Cu-Cu distances, closely matching those in Cu (FCC) metal. Our XAS data, which predict only a single nitrogen binding site (N2) and an in-plane inter-molecular distance of ca. 4 Å, suggests a topotactic relationship with Cu_2O (100) where the in-plane Cu-Cu distance is closely matched. The fact that there is no short (FCC type) Cu-Cu distance in this oxide surface perhaps explains the lack of surface binding to both the N1 and N2 (or N2 and N3) atomic sites.

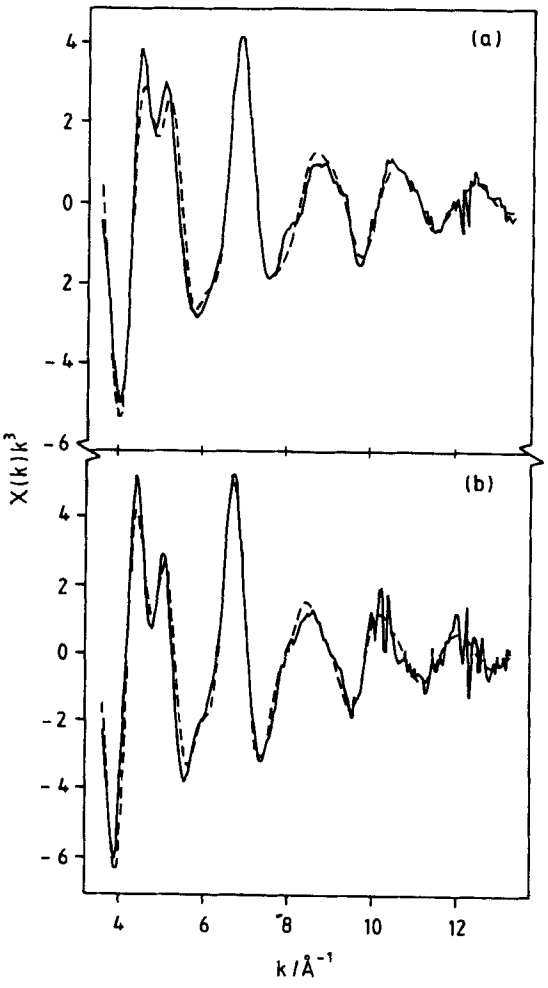

FIGURE 11. Experimental (——) and least-squares fitted (- - -) Cu K edge transmission EXAFS spectrum, after [28], of: (a) bulk Cu(I)-BTA; (b) Cu(I)-4-Br-BTA.

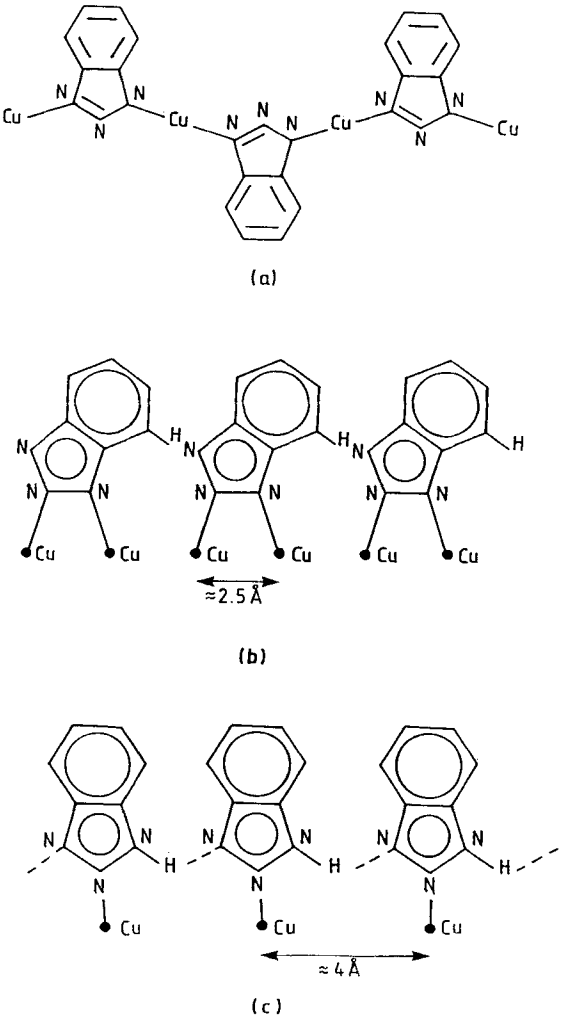

FIGURE 12. Structural models of the Cu(I)-BTA complex: (a) model proposed by Cotton and Scholes [30] for the bulk complex; (b) model proposed by Fang et al [33] for the coordination of BTA to a clean Cu surface; (c) model proposed for the coordination of BTA to an oxidised Cu surface, on the basis of the results of this investigation [28].

This example has shown how XAS (EXAFS at the Cu (8.98 keV) and Br (13.47 keV) K edges) can be used in a quantitative manner to characterise the molecular structure of an organo-metallic compound. It demonstrates the utility of multiple scattering calculations to resolve ring structures as well as the use of bromo-substitution techniques to provide a spectroscopic probe of proton sites in organic structures.

Structural Changes to Kaolinite Following Flash Calcination [34]

Kaolinite (china clay, $Al_2O_3.2SiO_2.2H_2O$) is one of the simpler members of a family of hydrated alumino-silicates and is of considerable commercial importance [35]. The kaolinite structure [36], as shown in figure 13, consists of alternate sheets of silicon tetrahedra and aluminium octahedra with Al coordinated to either oxygen or hydroxyl groups. The overall packing provides a lamellae-like structure involving a crumpled silica sheet mated to a squashed alumina sheet with successive sheet pairs van der Waals bonded together.

The endothermic dehydroxylation (calcination) of clay to produce metakaolin ($Al_2O_3.2SiO_2$) forms an important step in the manufacture of a range of clay products such as particulates for the paint and paper industries. Whilst the macroscopic aspects of this process are well known [37,38], our understanding of the atomistic processes taking place are quite limited [39,40]. This is due, in part, to the calcination process inducing extensive disruption to the clay structure; thus precluding structural characterisation by diffraction methods. The calcination process results in an explosive release of hydroxyl water, which in turn, causes the formation of voids associated with a marked decrease in bulk density and optical transparency. The latter reflects the fact that the void size

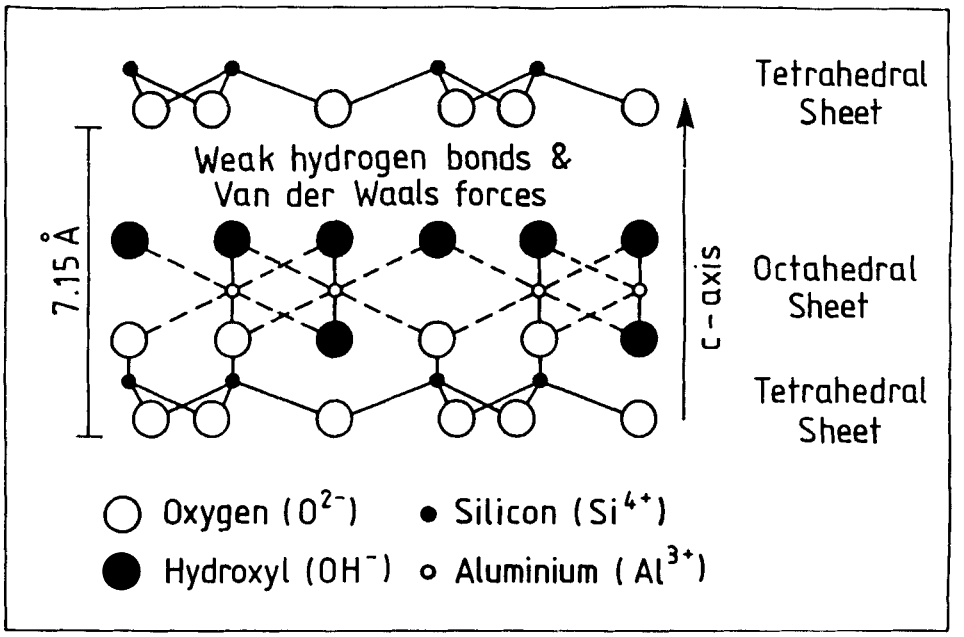

FIGURE 13. Schematic view of the atomic packing expected from a typical alumino-silicate such as kaolinite, after [34].

is commensurate with the wavelength of light; thus the exfoliated calcine is more opaque than conventionally produced materials. An understanding of structural change, as a function of calcination conditions, offers the potential to improve our control of void formation which should lead to improved particulate products.

In recent work [34] we have used electron yield XAS at the Al and Si K edges to probe changes to the clay structure following calcination. XAS data of the kaolinite and kaolinite calcines (1000°C in a He atmosphere for about 0.5 sec [41,42]) are shown in figure 14 (XANES) and Table 5 (EXAFS).

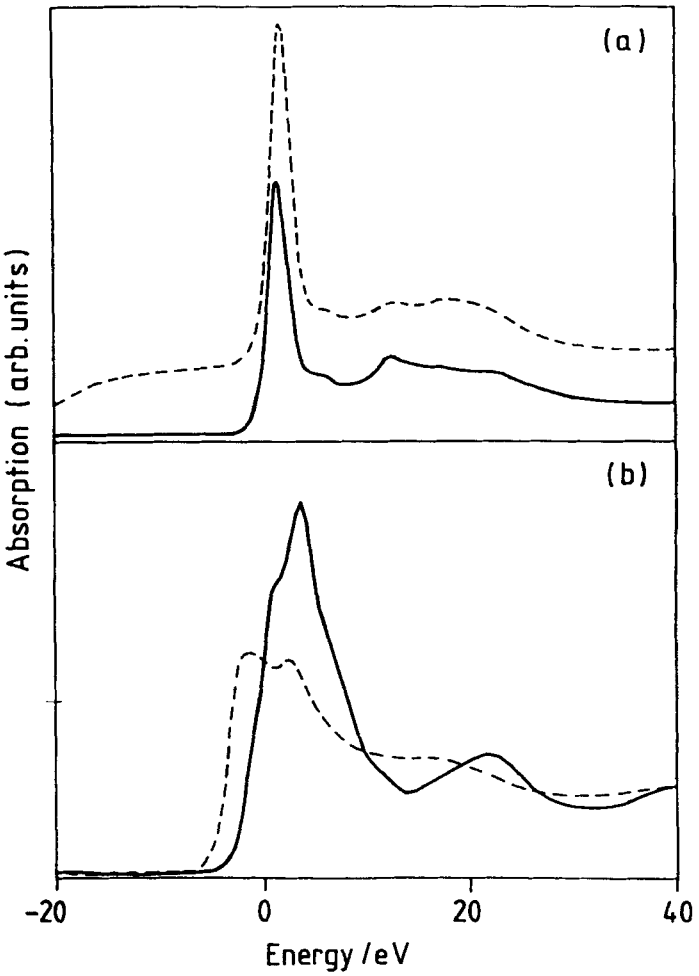

FIGURE 14. XANES spectra, after [34], taken at the Si (a) and Al (b) K edges for clays before (——) and after (-----) calcination.

	Al-O R/Å	Al-O N	Si-O R/Å	Si-O N
kaolinite	1.92	8.5	1.62	5.5
calcine	1.81	5.1	1.64	5.5

TABLE 5. Bond lengths (R) and coordination numbers (N) for Al and Si derived from fits to the EXAFS data for kaolinite before and after calcination, after [34].

The data taken at the Al absorption edge of clay before and after calcination reveal substantial changes to the environment around Al atomic sites associated with a change from Al in an octahedral (Al-O bond length ca. 1.92 Å) to a tetrahedral (Al-O bond length ca. 1.81 Å) coordination [43]. Changes to the Si K XANES spectra following calcination are more subtle, reflecting little substantial change to the Si local environment which remains similar to that found in tetrahedrally-coordinated Si minerals such as SiO_2. The Si K EXAFS analysis reveals some elongation of the Si-O bond following calcination, reflecting some relaxation in the inter-lamina region of this material.

In this example the use of soft XAS (EXAFS and XANES) in electron yield mode at the Al (1.56KeV) and Si (1.84KeV) to examine structural changes taking place in a typical alumino- silicate following calcination.

The Thermal Decomposition of Zinc Dialkyl Dithiophosphate (ZDDP) on Metal Surfaces [44]

For well over fifty years zinc dialkyldithiophosphate (ZDDP) [45] and related compounds, have been used as lubricating oil additives because of their attractive antiwear, antioxidant, corrosion inhibition and detergent properties [46]. Very little is known about the structural tribo-chemistry associated with this improved performance although previous studies have suggested that it is the decomposition products and not the ZDDP itself which mediate the additive action [47-49].

As part of a long term strategic study aimed at understanding the structural action of such additives, on the fundamental level, we examined the structure of a ZDDP mediated oil layer as adsorbed onto a mild steel surface before and after thermal decomposition at 135°C using XAS in the ultra-soft region arround the O K, Fe L and Zn L edges. The experimental set-up is given elsewhere [44,50,51]. The penetration depth of photons in this energy range is ca. 0.96 μm compared to ca. 13.4 μm and 5.6 μm thick, respectively, for the adsorbed and decomposed sample surfaces; thus the

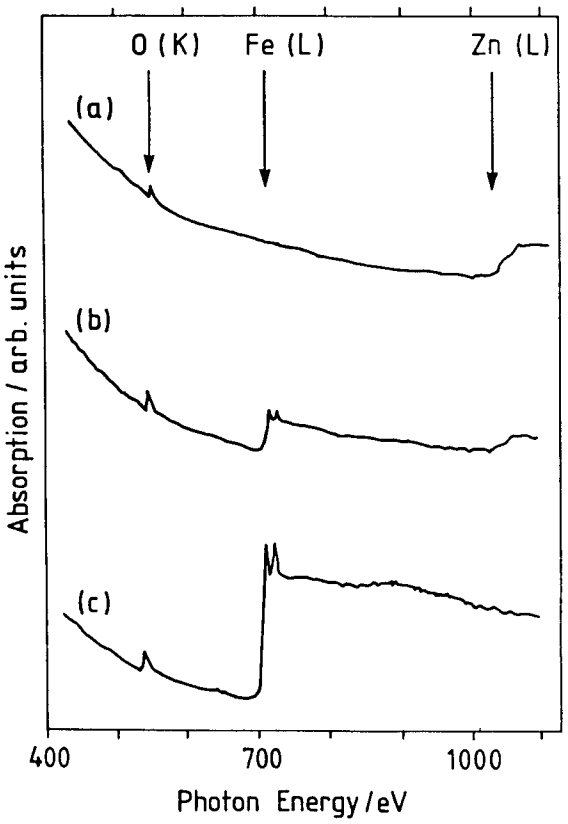

FIGURE 15. X-ray absorption spectra of ZDDP, after [44]: (a) coated onto steel, (b) adsorbed at 60°C and (c) adsorbed and decomposed at 135°C; spectra illustrates O K edge (540 eV), Fe L edge (710 eV) and Zn L edge (1020 eV).

measurements made reflect the structure of the adsorbed surface film.

An examination of the relative edge thresholds at the O K, Fe L and Zn L edges (figure 15) reveal that the adsorbed surface film before thermal treatment (b) contains Fe which is not found in the bulk oil (a). Additionally, the Zn threshold is reduced with respect to the oil. Following decomposition (c) Zn is no longer detected in the surface of the adsorbed film, whilst the Fe absorption threshold nearly doubles. Through an examination of the O K edge data with reference to well known model compounds (figure 16) it was found that the sample adsorbed at 60°C reflects a composition similar to that of ZDDP. Following decomposition at 135°C the data are consistent with a surface layer composition of FeO (25%), Fe_3O_4 (25%), $Zn_3(PO_4)_2$ (25%) and ZDDP (25%). The identification of Fe in the adsorbed layer implies cationic exchange is taking place between Fe^{2+} in the surface oxide and the Zn^{2+} in the ZDDP. This presence of an

enhanced Fe content coupled with the absence of any Zn species in the surface following decomposition suggest the formation of a layered interface with Zn close to the Fe substrate and the formation of an outer Fe containing layer. The structures involved in the decomposed layer are likely to include a mixture of phosphates, iron dialkyl dithiophosphates (FDDPs), polythiophosphates and oxides of iron.

This example has shown that fluorescence XANES in the ultra-soft region of the synchrotron radiation spectrum can be harnessed to examine structural change in the structure of an additive-mediated oil/metal(oxide) interface when operating under thermo-chemical conditions.

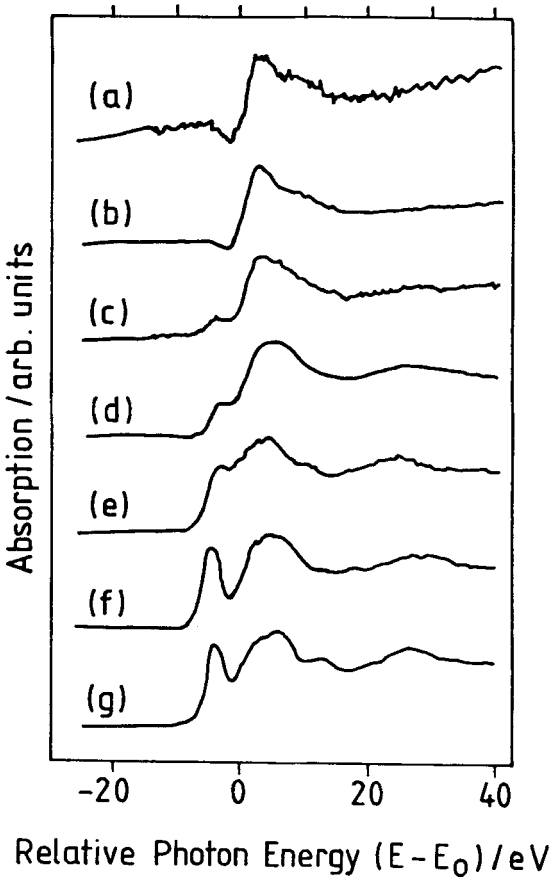

FIGURE 16. Oxygen near-edge spectra, after [44], of the model compounds together with the ZDDP surface films; (a) ZDDP, (b) ZDDP adsorbed at 60°C, (c) ZDDP adsorbed and decomposed at 135°C, (d) an Fe thin film, (e) FeO, (f) Fe_2O_3 and (g) Fe_3O_4.

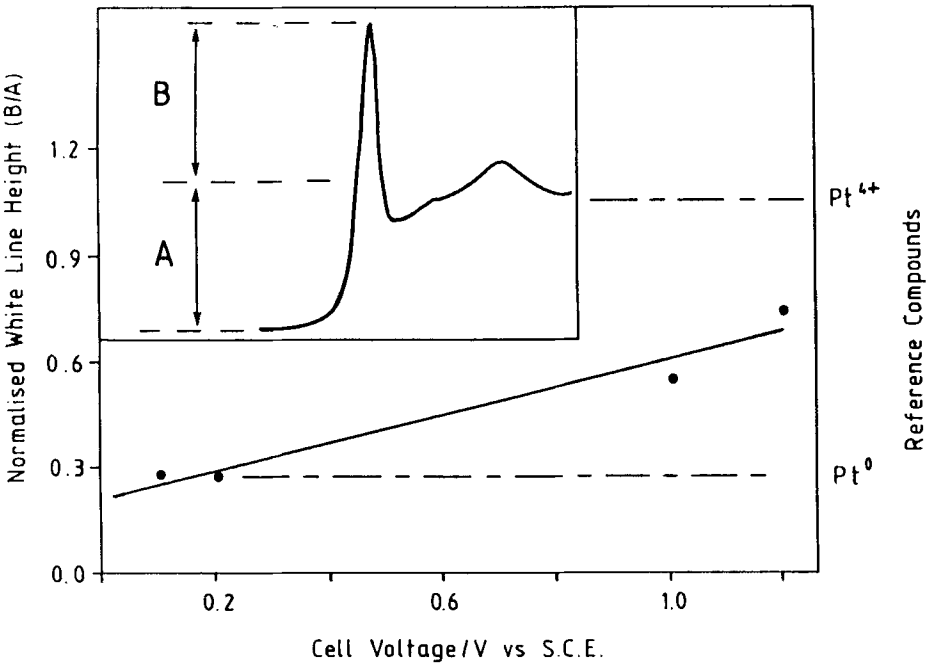

FIGURE 17. Normalised white line intensity ratio(B/A, see inset) derived from the Pt L3 near edge XAS spectra taken as a function of applied cell potential with reference to PtO2 and Pt foil standards, after [52-54].

The Local Atomic Structure of Pt Atoms in a Fuel Cell Electrode Operating under Potential Control [52-54]

There is a fundamental [55] and technological need [56,57] to understand the structural chemistry associated with oxygen adsorption on Pt electrode surfaces under electrochemical control. Whilst the use of conventional surface analysis techniques have provided much important information on these processes [58] they suffer from the disadvantage that the electrode surface has to be removed from its electrolyte for examination which may result in changes to the electrode surface chemistry.

To overcome such limitations [52-54] a Pt model fuel cell electrode (surface area ca. 238 m^2g^{-1}, particle size ca. 10 - 60 Å) was examined *in-situ* in a purpose-built electrochemical cell [59] using XAS at the Pt L edge. XAS data (figures 17 and 18) spectra were taken as a function of electrode potential probing the dispersed Pt structure from neutral (double-layer potential 0.10 V versus SCE) to oxidation conditions (1.20 V versus SCE). The XANES spectra (figure 16) reveals changes to the height of the absorption threshold maximum (the white line) which reflect [60] an increase in transitions to vacant d-shell orbitals when the electrode is oxidised; ie. the white line height in PtO_2 is much larger than in Pt metal. In the double-layer region (ca. 0.10 V)

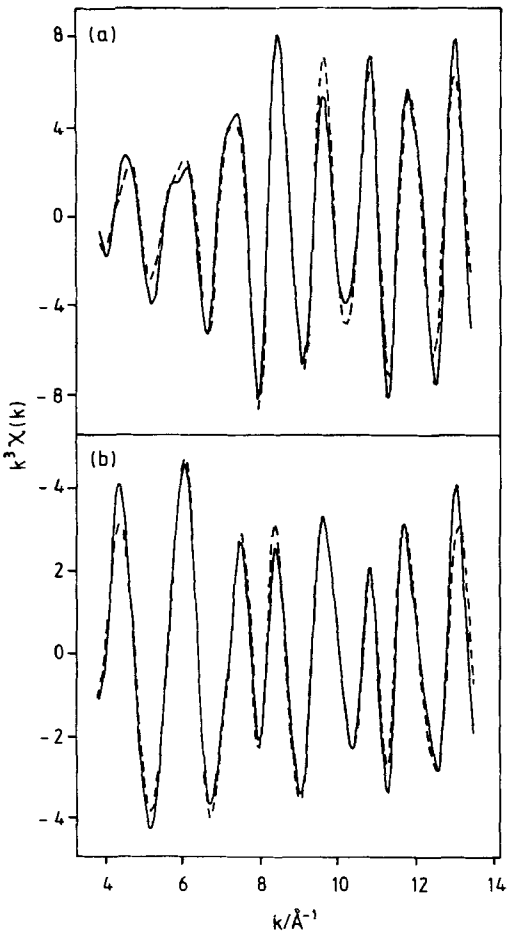

FIGURE 18. Experimental (_____) and best fitted (- - -) Pt L3 EXAFS spectra recorded *in-situ* from a Pt/C fuel cell electrode; (a) 0.10 V; (b) 1.20 V, after [52-54].

the electrode resembles metallic Pt with the data reflecting the enhanced oxidation of the Pt particles for increasing values of the electrode potential. At 1.20 V its height is smaller than that measured for a-PtO_2 reflecting the fact that the Pt particles are only partially oxidised.

An examination of the electrode structure in the double-layer region (0.10 V) shows (figure 18(a) and Table 6) the first three Pt neighbour (FCC) shell distances to be close to those in metallic Pt. Due to a small particle size (see figure 2(h)), the coordination numbers are lower than those of bulk Pt due to surface effects which are only significant for particle sizes much less than about 40 Å. This gives a particle size in its reduced

for the Pt/C electrode, in its reduced state at 0.10 V, to be about 10 - 16 Å. As the electrode potential is brought to the oxide formation region (ca. 0.80 V, figure 18(b)) the coordination numbers of the metallic-like shells decrease, going from 7.5 (for 0.10 V) to 2.9 (for 1.20 V) for the nearest neighbour Pt. Associated with this we see the formation of a Pt-O coordination for distances between 2.05 - 2.07 Å which are similar to that expected for α-PtO_2 and is consistent with Pt atoms octahedrally coordinated to oxygen. The absence of bulk oxide-like Pt-Pt coordinations at distances larger than 2.01 Å together with the existence of a large metal (FCC) fraction shows that only a thin oxide is formed. An average particle size in the "double-layer" region of 14 Å (ie containing 86 Pt atoms) is consistent with the formation of an oxide monolayer (ca. 2.2

Material	Particle size/Å	Atoms in Cluster	Oxide N_{OX}	Metal N1	N2	N3
Pt Metal	6	13	-	5.5	1.8	3.7
	8	19	-	6.3	1.9	5.1
	10	43	-	7.3	3.1	8.9
	12	55	-	7.9	3.3	9.6
	14	86	-	8.3	3.4	12.1
Electrode at 0.1 V vs S.C.E.	-	-	-	7.5	2.6	13.0
Electrode at 1.0 V vs S.C.E.	-	-	1.8	4.7	2.4	7.1
Oxidised Pt Particle	16.4	86	1.3	5.0	2.1	6.1
α-PtO_2			6.0	-	-	-
Pt Metal	16	141	-	8.8	3.9	13.6
	20	249	-	9.4	4.3	15.0
	∞	∞	-	12.0	6.0	24.0

TABLE 6. The calculated radial distribution functions around Pt atoms in spherical FCC clusters of variable diameter are compared with the nearest neighbour coordination numbers calculated from the EXAFS spectra (figure 18), after [52-54]; N1, N2 and N3 are the coordination numbers for the first three neighbour shells in metallic FCC platinum; N_{OX} is the coordination number for the first neighbour coordination shell in α-PtO_2; also included is the average coordination number expected when a 14 Å diameter Pt metal particle, consisting of 86 Pt atoms, is oxidised.

Å thick) at a cell potential of 1.00 V. The difference in densities between Pt metal (21.6 x 10^3 kg m^{-3}) [61] and oxide (10.9 kg m^{-3}) [62] results in an increase in the particle size from 14 Å to 16.4 Å on oxidation which increases the surface area of the particle by about 37%.

This example has shown that XAS (XANES and EXAFS at the Pt L edge (11.56 keV)) can be used to examine *in-situ* REDOX chemistry taking place on micro-porous Pt particles in an electrochemical cell when under potential control.

CONCLUSIONS AND FUTURE PERSPECTIVE

This brief overview has sought to describe the basic principles of X-ray absorption spectroscopy. It is hoped that the case examples detailed highlight the breadth of research possibilities, both in terms of experimental technique and application area, now accessible within solid-state, surface and structural chemistry.

There are many exciting developments in XAS techniques and applications, currently evolving within synchrotron radiation research groups; a full review of which is beyond the scope of this paper. Here, I would mention only one of these developments which uses the high photon flux provided by synchrotron radiation together with improved detector electronics so that XAS spectra can be collected in a few seconds. These quick-scanning XAS techniques [63], which open up the prospect of probing changes in chemical state dynamically, have been used to collect XANES spectra in time periods of ca. 4 s and EXAFS spectra in ca. 40 s [64]. In an *in-situ* study, the sucessive dehydroxylation, decomposition and reduction of $Ni(COOH).2H_2O$ (figure 19) was examined with the reaction temperatures for these solid-state reactions revealed (a) using differential scanning calorimetry (DSC). The reduction in data acquisition time ((b) and (c)) using the quick scanning technique now offers the exciting potential of combining XAS with DSC to provide a structural probe (d) capable of examining changes in oxidation state simultaneously with changes in the enthalpy associated with the structural change.

It is likely that the future will see a continuing demand for XAS and related synchrotron radiation techniques as reflected by the increase in the construction of dedicated electron storage rings, for synchrotron radiation research, worldwide. The availability of third generation electron storage rings, such as the European Synchrotron Radiation Facility, are bound to enhance our research opportunities using these techniques and move us into ever more challenging areas of structural chemistry.

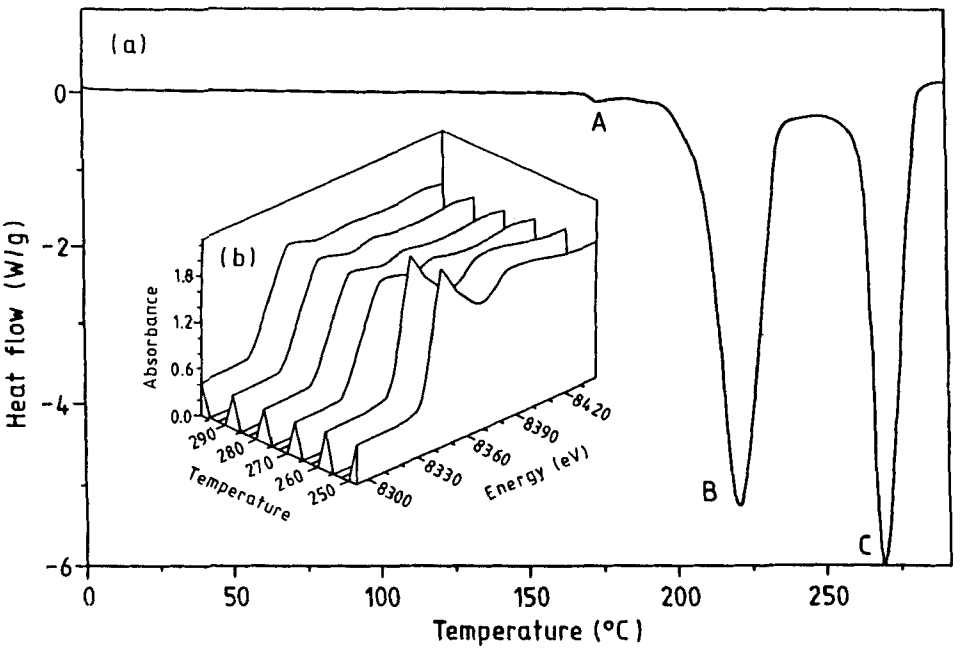

FIGURE 19. (a) DSC scan of Ni(COOH).4H_2O showing temperatures associated with the thermally-induced solid-state reactions (hydrated to anhydrous formate at 170°C (A), from anhydrous formate to oxide at 210°C (B) and oxide to metal at 270°C (C)); (b) quick-scanned XANES data (data acquisition time ca. 4 s) at the Ni K edge showing the thermally-induced reduction of NiO to metallic Ni at around 265°C, after [64,65]:

ACKNOWLEDGEMENTS

I gratefully acknowledge the SERC for the financial support of a senior fellowship and my numerous co-workers, as referenced in the original publications cited here, whose extensive work has enabled this overview to be presented. I am particularly grateful to the director and staff at the SERC's synchrotron radiation source at Daresbury Laboratory where much of the work described has been carried out. In recent years research on the structural characterisation of real interfaces has been supported through research, travel and studentship grants from the SERC, the British Council, ICI Chemicals and Polymers, Exxon Chemical and Johnson Matthey.

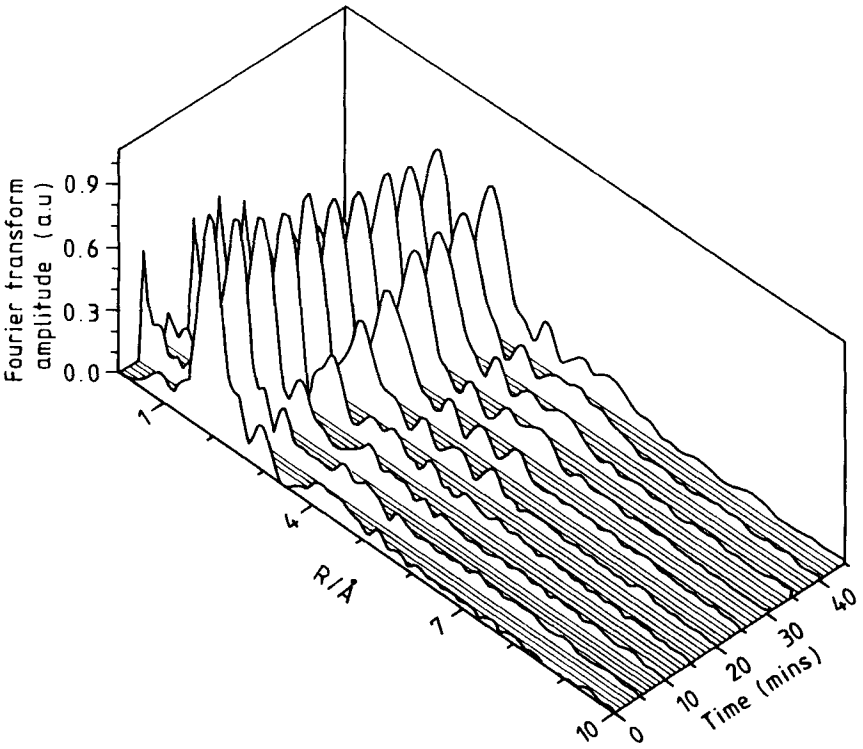

FIGURE 19(c). Fourier transformed quick scanned EXAFS data (100 ms integration time and scan speed 20 mdeg s^{-1}) recorded at the Ni K edge *in-situ* and isothermally in the meta-stable region close to C showing changes to the RDF following the slow thermal reduction of NiO to metallic Ni.

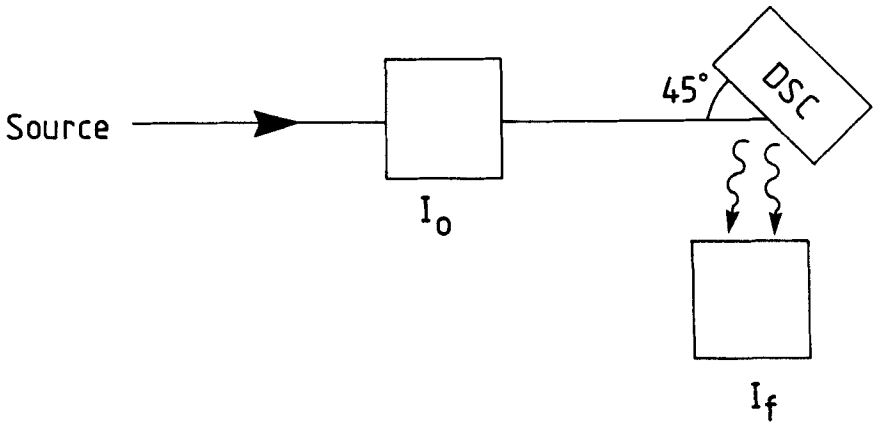

FIGURE 19(d). Schematic showing the experimental arrangement for combining XAS with DSC to provide a structural probe to examine oxidation state simultaneously with the thermodynamics of structural change.

REFERENCES

1. S Pizzini, K J Roberts, G N Greaves, N T Barrett, I D Dring and R J Oldman, In "Synchrotron Light: Applications and Related Instrumentation II", World Scientific Press, (1990), p67
2. D A H Cunningham, A R Gerson, K J Roberts, J N Sherwood and K Wojcieochowski, In "Advances in Industrial Crystallisation", (Editors J Garside, R J Davey and A G Jones), Butterworths, London, (1991), p105
3. A R Gerson, P J Halfpenny, S Pizzini, R Ristic, K J Roberts, D B Sheen and J N Sherwood, In "Material Science and Technology", Volume 2a, "Characterisation Techniques", (Editer E Lifshin), VCH Verlag, Weinheim, 1992
4. K J Roberts, J Crystal Growth 130 (1993) 657
5. J Schwinger, Phys Rev 75 (1949) 798
6. U Bonse, In "Characterisation of Crystal Growth Defects by X-ray Methods", (Edited B K Tanner and D K Bowen D K), Plenum Press, New York, (1979), p298
7. D E Sayers, F W Lytle and E A Stern, Adv in X-ray Anal, 13 (1970) 248
8. J B Hastings, In "EXAFS Spectroscopy", (Edited B K Teo and D C Joy), Plenum, New York, (1981), p171
9. T M Hayes and J B Boyce, Solid State Physics Vol 37, Academic Press, New York, (1982), p173
10. D E Koningsberger and R Prins, "X-Ray Absorption: Principles, Applications, Techniques of EXAFS, SEXAFS and XANES", (1988), Wiley
11. E A Stern and S M Heald, In "Handbook on Synchrotron Radiation", (Edited E E Koch) vol.1, North Holland, (1983)
12. M Hart, In "Characterisation of Crystal Growth Defects by X-ray Methods", (Edited B K Tanner and D K Bowen), Plenum Press, New York, (1979), p421
13. S J Gurman, J Phys C: Solid State Physics 21 (1988) 3699
14. A Bianconi, In "EXAFS for Inorganic Systems", (compiled by C D Garner and S S Hasnain), Report DL/SCI/R17 (SERC Daresbury Laboratory, Warrington WA4 4AD), (1982), p13
15. N T Barrett, G N Greaves, S Pizzini and K J Roberts, Surface Science 227 (1990) 337
16. S Pizzini, K J Roberts, G N Greaves, N T Barrett, I D Dring and R J Oldman, J Chem Soc Faraday Disc 89 (1990) 52
17. S Pizzini, "Characterisation of Real Surfaces and Condensed Interfaces using Glancing Angle X-ray Absorption Spectroscopy", PhD Thesis, University of Strathclyde, 1991
18. D R Armstrong, D A H Cunningham, K J Roberts and J N Sherwood, Proceedings 6th Int Conf X-ray Absorption Fine Structure (XAFS VI), Ellis Horwood (1991) 435
19. D A H Cunningham, D R Armstrong, G Clydesdale and K J Roberts, J Chem Soc Faraday Discussions 95 (1993) 347
20. D A H Cunningham, "Synchrotron Radiation Studies of Structural Aspects of Crystal Growth", PhD Thesis, University of Strathclyde, Glasgow, UK, 1991

21. G Clydesdale, K J Roberts and R Docherty, J Crystal Growth (1993) In press
22. H E Buckley, "Crystal Growth", 1951, Wiley, New York
23. J N Varghese and E N Maslen, Acta Cryst, B41 (1985) 181
24. E N Maslen, K J Watson and F H Moore, Acta Cryst, B44, (1988), 102
25. E O Schlemper and W C Hamilton, J Chem Phys, 44 (1966) 4498
26. T A Tyson, L Roe, P Frank, K O Hodgson and B Hedman, Phys Rev, B39 (1989) 6305
27. Pizzini, K J Roberts, I Dring, R J Oldman and G N Greaves, Proceedings of the 2nd European Conference on Progress in X-ray Synchrotron Radiation Research (Eds A Balerna, E Bernieri and S Mobilio), Società Italiane di Fisica, Conference Proceedings 25 (1990) 525
28. S Pizzini, K J Roberts, I S Dring, R J Oldman and D C Cupertino, J Materials Chemistry 3 (1993) 818
29. I Dugdale and J B Cotton, Corrosion Sci 3 (1963) 6
30. J B Cotton and I R Scholes, Brit Corrosion J 2 (1967) 1
31 J B Cotton, Proc 2nd Int Congr Metallic Corrosion (National Association of Corrosion Engineers, New York (1963) 590
32. C J Brown, J Chem Soc A (1968) 2488
33. B S Fang, C G Olson and D W Lynch, Surface Science 176 (1986) 476
34. K J Roberts, J Robinson, T W Davies and R M Hooper, Jap J Applied Physics 32-2 (1993) 652
35. W D Keller, Geology Today, July 1985, p109
36. see for example; R E Grim, Clay Minerology, McGraw-Hill, London 1968
37. J J Fripiat (Editor), "Advanced Techniques for Clay Mineral Analysis", Elsevier, 1982
38. J M Criado, A Ortega, C Real and E Torres de Torres, Clay Minerals 19 (1984) 653
39. C Otero-Arean, B C Gerstein and J J Fripiat, Proc Int Clay Conf, Bologna, Italy, (Elsevier) 1981
40. R H Meinhold, K J D Mackenzie and I W M Brown, J Mat Sci Lett 4 (1985) 1963
41. T W Davies, High Temperature Technology 2 (1984) 141
42. B Bridson, T W Davies and D P Harrison, Clays and Clay Minerals 33 (1985) 258
43. J Robinson, In "Proceedings of the Symposium on X-ray Methods in Corrosion and Interfacial Electrochemistry", The Electrochemical Society, New Jersey, (1992), p239
44. G P Hastie, K J Roberts, D Adams, D Fischer and G Meitzner, Jap J Applied Physics 32-2 (1993) 407
45. S L Lawton and G T Kokotailo, Inorg Chem 8 (1969) 2410
46. C N Rowe and J J Dickert, ASLE Trans, 10 (1967) 85
47. B Dacre and C H Bovington, ASLE Trans, 24 (1981) 546
48. B Dacre and C H Bovington, ASLE Trans, 26 (1982) 333
49. B Dacre and C H Bovington, ASLE Trans, 27 (1983) 252
50. M Sansone, R Hewitt, W Eberhardt and D Sondericker, Nucl Instrum Methods Phys Res, A266 (1988) 422

51. D A Fischer, J Colbert and J L Gland, Rev Sci Instrum, 60 (1989) 1596
52. S E Doyle, M E Herron, K J Roberts, J Robinson and F C Walsh, Proceedings 6th Int Conf X-ray Absorption Fine Structure (XAFS VI), Ellis Horwood (1991) 279
53. M E Herron, F C Walsh, S E Doyle, S Pizzini, K J Roberts, J Robinson and G Hards, J Electroanalytical Chemistry 324 (1992) 234
54. M E Herron, F C Walsh, S E Doyle, S Pizzini, K J Roberts and G Hards, Proceedings Symposium on the Use of X-ray Methods in Corrosion and Interfacial Electrochemistry, (Edited A J Davenport and J Gordon), The Electrochemical Society, New Jersey, Proceedings Volume 92-1 (1992) 171
55. L D Burke and M E G Lyons, In "Modern Aspects of Electrochemistry No 18", (Edited R E White, J O'M Bockris and B E Conway), Plenum, New York (1986), p169
56. A M Couper, D Pletcher and F C Walsh, Chemical Reviews, 90 (1990) 837
57. J O'M Bockris, B E Conway, E Jeager and R E White, Comprehensive Treatise of Electrochemistry Vol 3: Electrochemical Energy Conversion and Storage, Plenum Press, New York, 1981
58. R Parsons, In "Comprehensive Chemical Kinetics", (Edited R H Bamford and R G Compton), Vol 29, Elsevier, Amsterdam, 1988
59. M E Herron, S E Doyle, K J Roberts, J Robinson and F C Walsh, Rev Sci Instrum 63 (1992) 950
60. R J Oldman, J de Physique C8 (1986) 321
61. International Tables for X-ray Crystallography Volume 3, Kynoch Press, (1968), p282
62. H R Hoekstra, S Siegel and F X Gallagher, Adv Chem Ser 98 (1971) 41
63. R Frahm, Rev Sci Instrum, 60 (1989) 2515
64. B Edwards, C D Garner and K J Roberts, Proceedings of the 2nd European Conference on Progress in X-ray Synchrotron Radiation Research (Eds A Balerna, E Bernieri and S Mobilio), Società Italiane di Fisica, Conference Proceedings 25 (1990) 415
65. K J Roberts and D Adams, SERC Daresbury Laboratory Technical Memorandum DL/SCI/TM97E, 1993